Proton exchange membrane fuel cells powered with both CO and H$_2$

Xian Wang[a,b,1], Yang Li[a,b,1], Ying Wang[c,1], Hao Zhang[d,e,1], Zhao Jin[a], Xiaolong Yang[a,b], Zhaoping Shi[a,b], Liang Liang[a], Zhijian Wu[c], Zheng Jiang[d,f], Wei Zhang[g] ⓘ, Changpeng Liu[a,b], Wei Xing[a,b], and Junjie Ge[a,b,2]

[a]State Key Laboratory of Electroanalytic Chemistry, Jilin Province Key Laboratory of Low Carbon Chemistry Power, Changchun Institute of Applied Chemistry, Chinese Academy of Sciences, Changchun 130022, P. R. China; [b]School of Applied Chemistry and Engineering, University of Science and Technology of China Hefei 230026 P. R. China; [c]State Key Laboratory of Rare Earth Resource Utilization, Changchun Institute of Applied Chemistry, Chinese Academy of Sciences, Changchun 130022 P. R. China; [d]Shanghai Institute of Applied Physics, Chinese Academy of Sciences, Shanghai 201204 P. R. China; [e]Shanghai Institute of Applied Physics, University of Chinese Academy of Sciences, Beijing 100049, P. R. China; [f]Shanghai Synchrotron Radiation Facility, Zhangjiang National Lab, Shanghai Advanced Research Institute, Chinese Academy of Sciences, Shanghai 201204 P. R. China; and [g]Electron Microscopy Center, Key Laboratory of Automobile Materials Ministry of Education, School of Materials Science & Engineering, Jilin University, Changchun 130022 P. R. China

The CO electrooxidation is long considered invincible in the proton exchange membrane fuel cell (PEMFC), where even a trace level of CO in H$_2$ seriously poisons the anode catalysts and leads to huge performance decay. Here, we describe a class of atomically dispersed IrRu-N-C anode catalysts capable of oxidizing CO, H$_2$, or a combination of the two. With a small amount of metal (24 μg$_{metal}$·cm^{-2}) used in the anode, the H$_2$ fuel cell performs its peak power density at 1.43 W·cm^{-2}. When operating with pure CO, this catalyst exhibits its maximum current density at 800 mA·cm^{-2}, while the Pt/C-based cell ceases to work. We attribute this exceptional catalytic behavior to the interplay between Ir and Ru single-atom centers, where the two sites act in synergy to favorably decompose H$_2$O and to further facilitate CO activation. These findings open up an avenue to conquer the formidable poisoning issue of PEMFCs.

fuel cell | hydrogen oxidation reaction | antipoisoning | single atomic sites synergy

The proton exchange membrane fuel cell (PEMFC) is one of the key enabling technologies for the transition to the upcoming hydrogen economy (1–9). However, PEMFCs have their Achilles' heel, i.e., they are easily poisoned by carbon monoxide (10–12). The platinum catalysts, being used exclusively to drive the fuel cell anode, bind to CO preferentially (1 ppm CO in H$_2$ causes >90% surface blockage) and cease to catalyze hydrogen oxidation due to site blockage (13–16). This feature of Pt makes the use of cheap crude H$_2$ (~US$1.5·kg^{-1}) from steam reforming unrealistic, and the fuel cell vehicles (FCVs) are now fed exclusively with pure or purified H$_2$ at ~10 times higher price (~US$13 to16·kg^{-1}).

To prompt the widespread application of PEMFCs, the anode catalysts should possess certain antipoisoning behavior (17–21), as the H$_2$ quality may not always be fully assured in each time of refilling. The exploration for less CO-sensitive anode catalysts has been around since the emergence of the PEMFC technology (2, 3, 5). Various Pt-based alloys were explored to alleviate the CO poisoning through the Langmuir–Hinshelwood reaction mechanism (21, 22). However, impractically high voltage losses (0.2 to 0.5 V) are still evident in the presence of trace level CO (10 to 1,000 ppm), owning to the intrinsically too strong CO adsorption on the current metallic Pt catalysts. Therefore, designing catalytic sites with reduced CO adsorption energy is highly desirable for tackling such a problem. Meanwhile, as water is also the reactant for CO electrooxidation, specific catalytic sites capable of activating water at a sufficiently low potential is demanded (23, 24). However, these stringent requirements have not been met by the currently available catalysts yet. For instance, PtRu/C, the best CO tolerant catalysts to date, requires a high Pt usage (normally >0.4 mg·cm^{-2}) to afford for a certain cell performance in a CO presence

(25, 26), which runs in the opposite direction to the cost reduction demand of the technique.

Herein, we report a class of IrRu-N-C catalysts, with Ir and Ru single atoms densely and uniformly populated in nitrogen–carbon composites. The catalyst represents an example of high-efficiency single-atom catalysis in an H$_2$ fuel cell with practical power density. Meanwhile, the Ir and Ru single sites act in synergy to fast catalyze the CO electrooxidation reaction (COOR), where both CO and H$_2$O are sufficiently activated at a low potential. Therefore, the IrRu-N-C catalyst at ultralow metal loading exhibits even better antipoisoning behavior (10 to 1,000 ppm CO) than the PtRu/C catalysts that is 17 times higher in mass loading (0.4 mg·cm^{-2}). Our results thus suggest a promising bimetal center design strategy for producing active and antipoisoning hydrogen oxidation reaction (HOR) catalysts for PEMFC anodes.

Results

Structural Characterization. We fabricated the catalysts through pyrolyzing (950 °C) zeolite imidazolate frameworks 8 (ZIF-8) trapped with ruthenium acetylacetonate and iridium acetylacetonate

---

Significance

We report a class of IrRu-N-C catalysts, with Ir and Ru single atoms uniformly populated in nitrogen–carbon composites. The catalyst not only represents an example of high-efficiency single-atom catalysis toward H$_2$ electrooxidation, but also exhibits excellent CO electrooxidation reaction (COOR) behavior. The traditionally invincible CO electrooxidation process occurs easily on this catalyst, with COOR initiates at nearly 0 mV versus reversible hydrogen electrode at ambient temperature. This endows the catalyst with superb CO antipoisoning property in proton exchange membrane fuel cell at ultralow noble metal loading. Combining theoretical calculation and physical probing techniques, we find that the approximated Ir and Ru single atomic sites act in synergy to confer the catalysts with this excellent CO conversion behavior.

CHEMISTRY

(Fig. 1*A*), i.e., the host guest strategy (27–29). The metal loading in the final catalysts was systematically tuned to obtain optimized catalysis behavior (Ir, 0 to 1.1 wt%, Ru, 0 to 0.6 wt%, *SI Appendix*, Table 1), with selected samples hereafter denoted as Ir-N-C (1.1 wt%), IrRu-N-C (Ir and Ru both at 0.6 wt%), and Ru-N-C (0.6 wt%). The Ir(acac)$_3$ and Ru(acac)$_3$ molecules were in situ trapped in the cages formed by the assembly of Zn^{2+} ions and 2-methyl imidazole. Using aberration-corrected high-annular dark-field scanning transmission electron microscopy (HAADF-STEM), the Ir and Ru are shown to be atomically confined in the micropores of ZIF-8, as indicated by the isolated starry spots in the substrate (Fig. 1 *B* and *C*). The polyhedron morphology (*SI Appendix*, Fig. 1) and well-maintained crystalline texture (Fig. 1*D* and *SI Appendix*, Fig. 2*A*) of the IrRu@ZIF-8 in comparison with pristine ZIF-8 verifies the host−guest structure of IrRu@ZIF-8. The following pyrolysis leads to sample carbonization, as indicated by the X-ray diffraction (XRD) patterns (Fig. 1*D* and *SI Appendix*, Fig. 2*B*), where only two broad peaks located at 25° and 44° assignable to the characteristic carbon (002) and (100) diffractions
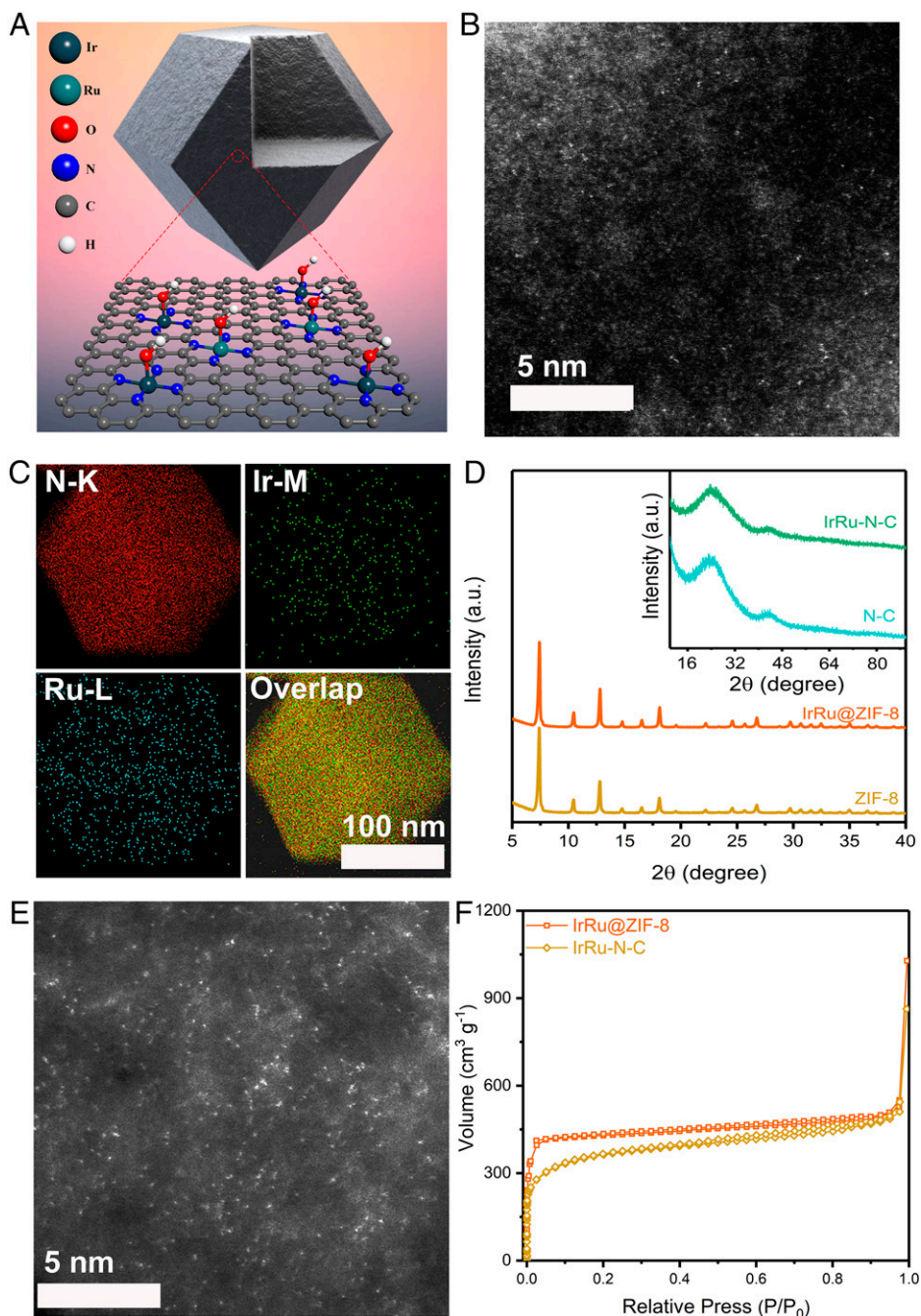

Fig. 1. The physical characterizations. (*A*) Schematics of IrRu-N-C catalysts. (*B*) The HAADF-STEM image of IrRu@ZIF-8, indicating the single-atom dispersion nature of Ir and Ru in the ZIF-8 precursor. (*C*) Energy-dispersive X-ray elemental mapping of IrRu@ZIF-8. (*D*) XRD patterns of precursors (IrRu@ZIF-8 and ZIF-8) and catalysts (IrRu-N-C and N-C). The broad peaks at around 20 to 30° and 40 to 50° can be assigned to the amorphous carbon. (*E*) HAADF-STEM image of IrRu-N-C, indicating the predominant atomic dispersion of Ir and Ru in the final catalyst. (*F*) Typical N$_2$ adsorption–desorption isotherms of IrRu@ZIF-8 and IrRu-N-C.

are noticed in all carbonized samples. N_2 adsorption/desorption results (Fig. 1F and *SI Appendix*, Fig. 3 and Table 2) show that the IrRu-N-C, Ir-N-C, and Ru-N-C catalysts all represent surface area and pore structure similar to the N-C (derived from ZIF-8) catalyst. Energy-dispersive spectrum elemental mappings indicate metal species, nitrogen, and carbon are still homogeneously distributed throughout the sample (*SI Appendix*, Figs. 4–8). Using HAADF-STEM (Fig. 1E), the Ir and Ru sites are revealed to maintain their atomic dispersion status (named IrRu-N-C) after carbonization, with densely planted bright dots noticed due to Z-contrast. Small amount of tiny particles are also noticed in the samples, which are revealed as Ru metallic entities (*SI Appendix*, Fig. 6).

To further unveil the coordination and electronic nature of Ir and Ru in IrRu-N-C, we then resorted to extended X-ray absorption fine structure (EXAFS) and X-ray absorption near edge structure (XANES) spectroscopy (Fig. 2 A–F). First, Ir L_3-edge EXAFS results support the single-atom nature of Ir sites in the catalysts (Ir-N-C and IrRu-N-C). The phase uncorrected Fourier transform EXAFS (FT-EXAFS) results show a single prominent peak located at 1.5 Å ascribable to Ir-N/O back scattering (Fig. 2 A–C), with a metallic Ir-Ir scattering path (2.4 Å) being absent. Least-squares FT-EXAFS curve-fitting analysis shows an average coordination number (CN) of 5.1 and a bond length at 2.02 Å (*SI Appendix*, Table 3) of the Ir-N/O. Second, the Ru K-edge FT-EXAFS results corroborate the coexistence of single-atom Ru species (Ru-N/O path at 1.5 Å) and Ru metallic particles (Ru-Ru path at 2.5 Å) (Fig. 2E and *SI Appendix*, Table 4). The Ru fraction engaged as metallic

particles is calculated as 19% (*SI Appendix*, section 1.13), with isolated Ru revealed as the dominant structure in the sample (81%). The fitting analysis shows an average CN at 5.3 and the bond length at 2.03 Å of the Ru-N/O path. From here, we confirm that Ir and Ru single atom sites dominant the sample, as further supported by the XAFS wavelet transform (WT) analysis in k-space resolution (*SI Appendix*, Figs. 9 and 10). Meanwhile, the overall CN for Ir-N/O and Ru-N/O at around 5 implies H_xO-IrN$_4$ and H_xO-RuN$_4$ as the most possible site configuration. Third, Ir L_3-edge XANES white line intensity (Fig. 2 B and C), signifying the transition from occupied 2p to empty 5d states, indicates an average extrapolated valence at +3 ($5d^6 6s^0$) (30–32), consistent with XPS results (*SI Appendix*, Figs. 11–13 and Table 5). Ru K-edge XANES profiles (Fig. 2D) reveal that Ru is also positively charged on average, with edge signals located between Ru foil and RuO_2. These results are in line with the EXAFS analysis, where the metal centers are in cationic states resembling those of the metal porphyrins.

Electro-Catalysis Behavior in Acidic Electrolytes. We then tested the HOR performance of the catalysts, using the best HOR catalysts to date (i.e., the commercial Pt/C and Ir/C catalysts) as benchmarks (*SI Appendix*, Fig. 14). First, the Pt/C catalyst exhibits typical HOR behavior, with kinetic behavior and diffusion-limiting current resembling those in the calculation results from the Levich equation (*SI Appendix*, section 1.14) and literature (33, 34). The lower diffusion-limiting current on Ir/C than on Pt/C may arise from the surface oxidation of Ir and thereby the lowered true active site density. Second, the
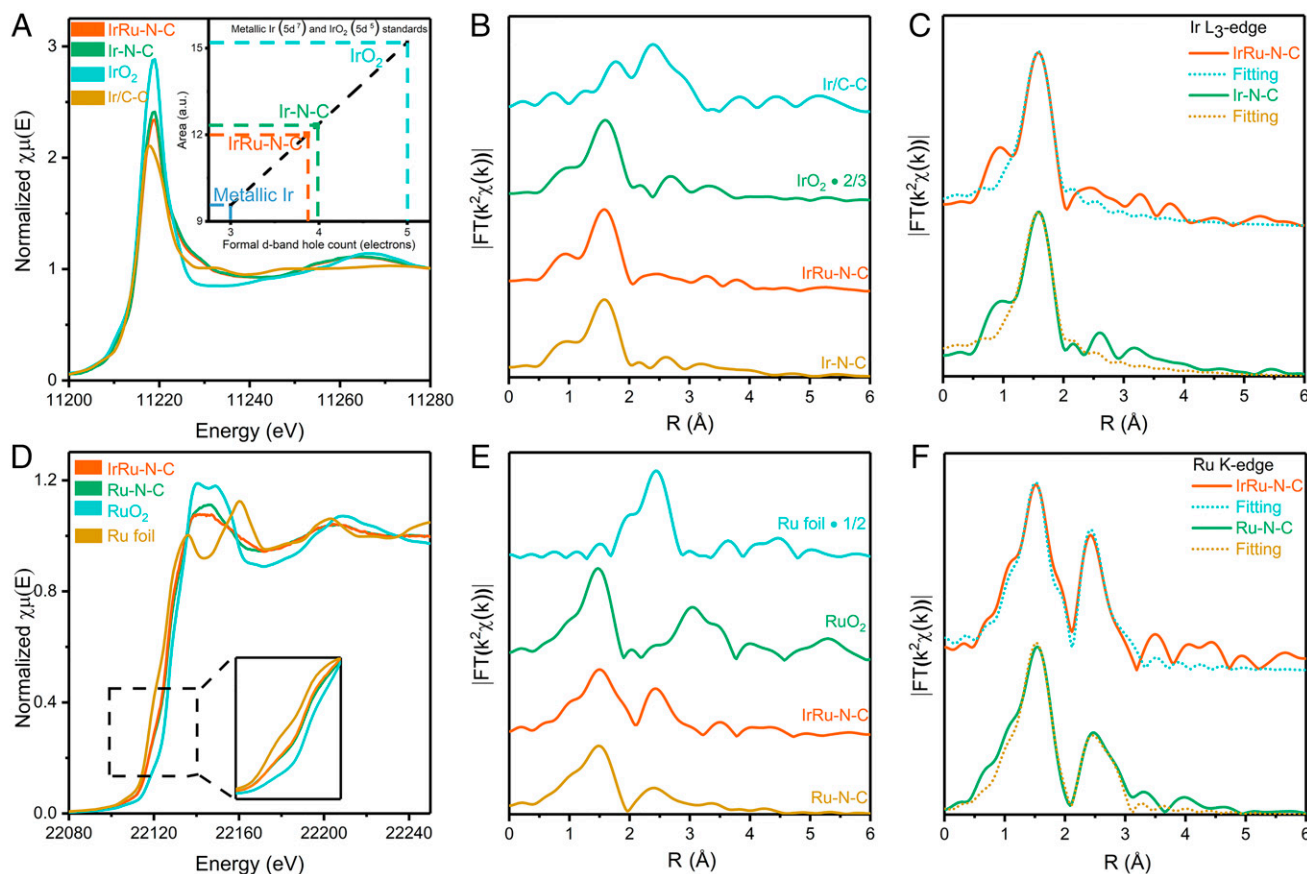

Fig. 2. Structural analyses. (A) XANES of Ir L_3-edge spectra; the inset is used to confirm the Ir valence by L_3-edge area integration. (B) Fourier transform of k^2-weighted Ir L_3-edge EXAFS data. (C) Experimental and best-fitting IrRu-N-C and Ir-N-C results of the Ir L_3-edge EXAFS. (D) XANES of Ru K-edge spectra; the inset is used to evaluate the Ru valence. (E) Fourier transform of k^2-weighted Ru K-edge EXAFS data. (F) Experimental and best-fitting IrRu-N-C and Ir-N-C of the Ru K-edge EXAFS results.

Wang et al.
Proton exchange membrane fuel cells powered with both CO and H_2

PNAS | 3 of 7
https://doi.org/10.1073/pnas.2107332118

IrRu-N-C catalyst represents HOR kinetic behavior resembling the Pt/C electrode, demonstrating their highly efficient HOR catalysis nature. A higher diffusion-limiting current is evidenced on the IrRu-N-C electrode (i.e., 3.6 mA·cm^{-2} versus the calculated 2.93 mA·cm^{-2}) from the Levich equation. This result is well reproduced across samples, with an SD at only 6.2% (*SI Appendix,* Fig. 15). This phenomenon has also been reported previously (35, 36) and can be attributed to the formation of a porous three-dimensional thick electrode due to the high overall loading of the catalyst (0.51 mg·cm^{-2} catalyst and 6.0 μg·cm^{-2} metal loading). Notably, the thickness of IrRu-N-C electrode film is 28 μm according to three-dimensional profile evaluation (*SI Appendix,* Fig. 16), far exceeding the Pt/C catalyst film at 3.7 μm, and thereby results in a diffusion-limiting current exceeding the theoretical value calculated from the Levich equation. Third, neither Ru-N-C nor N-C catalyst show distinct HOR catalytic behavior, while Ir-N-C shows inferior HOR catalytic activity, thus suggesting the Ir center as the catalyst site and Ru as the promoter. Through HOR performance comparison, we show that IrRu-N-C exhibits comparable HOR behavior to the-state-of-the-art Pt/C catalyst, at a much lower metal loading (6 μg$_{metal}$·cm^{-2} versus 20 μg$_{metal}$·cm^{-2}).

Having achieved satisfactory HOR performance, we then turned to investigate the carbon monoxide oxidation behavior of all of the catalysts in the CO-saturated electrolyte, as it will largely determine the antipoisoning feature of the catalysts (Fig. 3A and *SI Appendix,* Fig. 17). Expectedly, the Pt/C catalysts do not catalyze CO oxidation until the electrode potential reaches 0.8 V versus reversible hydrogen electrode (RHE), in line with the literature (25, 26). On the commercial PtRu/C, which is recognized as the best CO-tolerating anode catalyst, the CO electrooxidation reaction (COOR) initiates at ∼0.5V, in good agreement with literature (13–16). To our surprise,

however, the IrRu-N-C exhibits excellent COOR activity, which reaches its half-wave potential (E$_{1/2}$) at 50 mV versus the RHE and diffusion-limiting current at ∼100 mV, respectively. The CO to CO$_2$ conversion is further verified by online mass spectrometry (MS). As shown in Fig. 3B and *SI Appendix,* Figs. 18–20, the concurrent mass spectrometric signal at m/z = 44, corresponding to CO$_2$, is unambiguously shown with the electrode potential set at 25, 50, 100, and 200 mV versus RHE for 5 s in the CO-saturated electrolyte, respectively, corroborating the low potential COOR feature of our catalyst. The overall charge transfer number for the COOR is calculated at ∼2.00 using the Levich equation (*SI Appendix,* section 1.14) in the diffusion-limiting current region, corresponding to the complete conversion from CO to CO$_2$ (Eq. **1**). As water also participates in the reaction, this result implies that both CO and H$_2$O are activated on the IrRu-N-C sample at a sufficiently low potential, thereby endowing the catalyst with this excellent CO oxidation behavior. We then carried out further experiments to distinguish the function of Ir from Ru in activating CO and H$_2$O. The Ru-N-C does not catalyze CO electrooxidation at all, while Ir-N-C shows a much inferior CO electrooxidation activity (E$_{1/2}$ at 0.31 V versus RHE) in the absence of Ru sites (Fig. 3A and *SI Appendix,* Fig. 19). We thus deduce that Ir atoms are the COOR catalytic center, while Ru may work cooperatively to facilitate H$_2$O dissociation or boost the CO oxidation, as further discussed in the theoretical calculation part.

$$CO + H_2O = CO_2 + 2H^+ + 2e^- \qquad [1]$$

We then tested the performance of the IrRu-N-C catalysts in PEMFC single cells with or without CO presence under varied testing conditions (Fig. 3 C–E and *SI Appendix,* Fig. 21 and Table 6), using commercial Pt/C and PtRu/C as the reference. Firstly, the HOR performance of the IrRu-N-C catalyst is
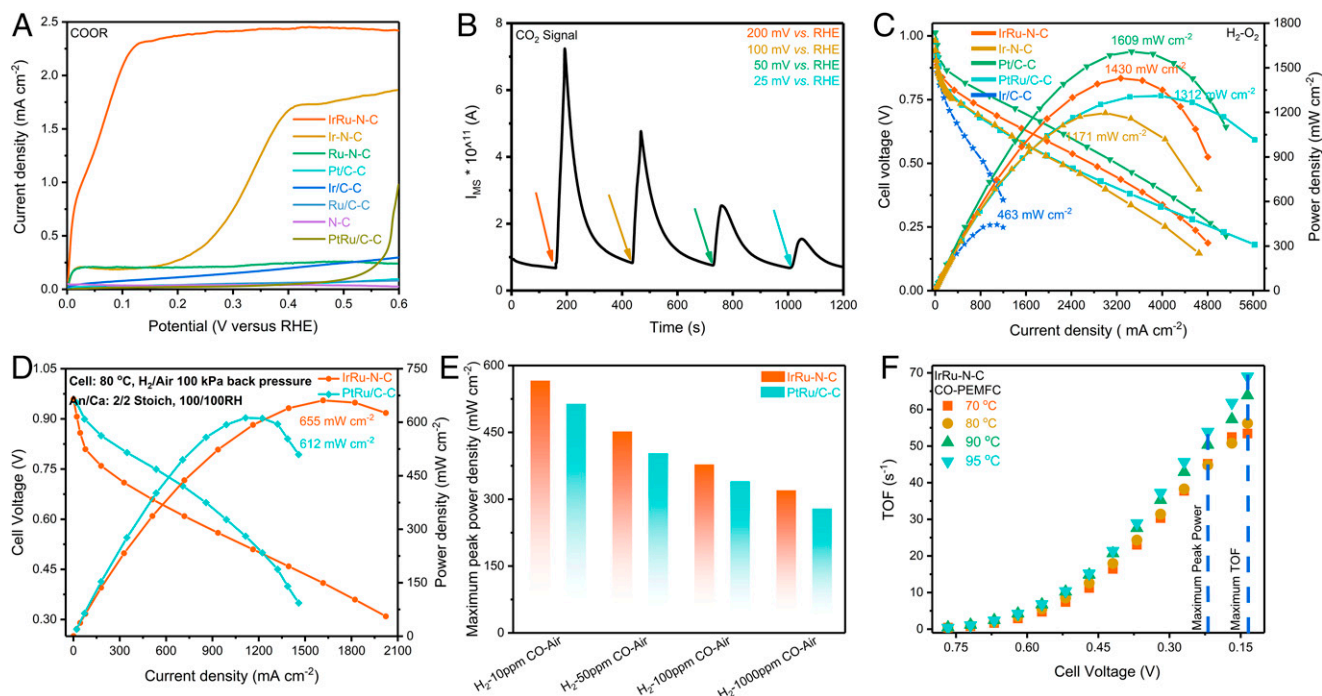

Fig. 3. H$_2$/CO electrooxidation and fuel cell test results of the different catalysts. (A) COOR linear sweep voltammetry (LSV) curves with the scanning rate at 20 mV·s^{-1} and rotating speed at 1,600 rpm on RDE. (B) The IrRu-N-C catalysts' signals of CO$_2$ in a thin-layer online MS cell in the presence of saturated CO in 0.1 M HClO$_4$ at different potential. (C) H$_2$-O$_2$ PEMFC cell performance of different anode catalysts at 95 °C with 200 kPa back pressure and 100% RH with metal loading 24 μg$_{metal}$·cm^{-2} (IrRu-N-C and Ir-N-C), 0.1 mg$_{metal}$·cm^{-2} (Pt/C), and 0.4 mg$_{metal}$·cm^{-2} (PtRu/C), respectively. (D) H$_2$-Air PEMFC cell performance of 24 μg$_{metal}$·cm^{-2} IrRu-N-C and 0.4 mg$_{metal}$·cm^{-2} (PtRu/C) at 80 °C with 100 kPa back pressure and 100% RH. (E) H$_2$-x ppm (x = 10, 50, 100, 1,000) CO-Air PEMFC maximum peak power density of 24 μg$_{metal}$·cm^{-2} IrRu-N-C and 0.4 mg$_{metal}$·cm^{-2} (PtRu/C) at 80 °C with 50 kPa back pressure and 100% RH. (F) TOF of IrRu-N-C at different temperatures at CO atmosphere.

validated by running the fuel cell under H_2-O_2 mode. Specifically, the cell using IrRu-N-C (24 $\mu g_{metal}\cdot cm^{-2}$) anode exhibits peak power density at 1.43 $W\cdot cm^{-2}$, comparable to the Pt/C and PtRu/C catalyst at a much higher metal loading (1.61 $W\cdot cm^{-2}$ and 1.31 $W\cdot cm^{-2}$, 0.1 $mg_{metal}\cdot cm^{-2}$ and 0.4 $mg\cdot cm^{-2}$, respectively) at the same operating conditions (95 °C, 100% relative humidity [RH], and 200 kPa back pressure), as shown in Fig. 3C. The maximum current density reaches 4.8 $A\cdot cm^{-2}$, indicating that the H_2 electrooxidation occurs satisfactorily fast on IrRu-N-C at ultralow metal loading. The Ru-N-C, however, is not an active anode catalyst in the fuel cell device, which is consistent with the electrochemical test (*SI Appendix*, Fig. 14). Secondly, the single-cell performances of IrRu-N-C- and PtRu/C-based anodes were compared systematically under both H_2-O_2 and H_2-Air mode at varied testing conditions, as shown in *SI Appendix*, Table 6. Notably, in spite of that the IrRu-N-C anode is only one-seventeenth in the metal loading of that of the PtRu/C (24 $\mu g_{metal}\cdot cm^{-2}$ versus 0.4 $mg\cdot cm^{-2}$), it exhibits superior performance than the counterpart PtRu/C at all testing conditions. For instance, at US Department of Energy operating conditions (H_2-Air mode, 80 °C, 100% RH, and 50 to 200 kPa back pressures) (37), our IrRu-N-C catalyst represents peak power densities at 592 to 787 $mW\cdot cm^{-2}$, which is higher than the PtRu/C catalysts (578 to 736 $mW\cdot cm^{-2}$) at a much higher anode loading, as shown in *SI Appendix*, Table 6 and Fig. 3D. Taking into account the significantly lowered metal loading, our catalyst is ~18 times in mass activity that of the PtRu/C. Lastly and most importantly, under exposure to varied content of CO (10 to 1,000 ppm), the excellent antipoisoning feature of IrRu-N-C is further elucidated. Notably, when tested under H_2-Air mode in CO presence(80 °C, 100% RH, and 50 kPa back pressure), the PtRu/C catalyst (0.4 $mg\cdot cm^{-2}$) represents peak power densities varying between 514 and 279 $mW\cdot cm^{-2}$ (CO concentration between 10 and 1,000 ppm), similar to those reported in the literature (26, 38–41). However, despite of the significantly lowered metal loading, our IrRu-N-C catalyst represents higher peak power densities at all CO concentrations (i.e., 566 through 320 $mW\cdot cm^{-2}$) (Fig. 3E, and *SI Appendix*, Fig. 22). These results unambiguously suggest the better CO tolerance of our catalyst, which is 18.4 to 19.1 times in mass activity that of PtRu/C, the catalysts in the CO presence. Therefore, the IrRu-N-C represents an antipoisoning feature that has not been possible with the previously reported PEMFC catalysts (*SI Appendix*, Table 7).

Having achieved high CO tolerance in the PEMFC single cell, we further run the fuel cell under a more challenging condition (i.e., feeding the cell exclusively with humidified CO as fuel) to see the difference between the varied catalysts (*SI Appendix*, Fig. 23). As expected, the Pt/C and Ir/C anodes completely cease to work in pure CO, due to the full coverage of CO on the Pt and Ir nanoparticles. Even on the PtRu/C catalysts, a peak power density at only 30 $mW\cdot cm^{-2}$ is achieved, due to the great difficulty and the high overpotential in CO oxidation on the PtRu alloy. Using our IrRu-N-C anode, however, the single cell exhibits its peak power density at 166 $mW\cdot cm^{-2}$, with maximum COOR current density reaching 800 $mA\cdot cm^{-2}$. Assuming all the Ir atoms are active, the CO turnover frequency (TOF) is calculated at 68.6 s^{-1} (Fig. 3F), 1 to 2 orders of magnitude higher than the best CO chemical and electrochemical oxidizing catalysts in the same temperature range (12, 23, 24, 42). We again attribute this excellent COOR feature to the interplay between Ir and Ru, as the cell based on Ru-N-C is null and the one with Ir-N-C exhibits a much inferior performance (41 $mW\cdot cm^{-2}$).

Catalytic Stability Evaluation. Catalytic stability is another prominent concern for catalysts used in fuel cell applications. We first investigated the durability of the catalyst using rotating disk electrode (RDE), where the potential was cycled between 0 and 0.4 V versus RHE, in H_2- or CO-purged 0.1 M $HClO_4$ electrolyte for 10,000 cycles. As shown in *SI Appendix*, Fig. 24, no obvious decay in either the kinetic region or in the diffusion-limiting current was observed in the H_2-purged condition after the accelerated durability tests. In the COOR test, the $E_{1/2}$ only slightly increases from 44 to 51 mV, with the diffusion-limiting current staying almost unchanged. We then collected the IrRu-N-C catalysts for the HAADF-STEM to investigate the morphology after the RDE test. As shown in *SI Appendix*, Fig. 25, the single-atom dispersed Ir and Ru remain intact after the durability test, suggesting the robustness of the catalyst structure.

We further carried out the stability test of the catalyst in PEMFC, under constant voltage mode at 0.65 V under 100 kPa H_2-O_2, combined with start-up/shut-down cycles (13 h a day) and N_2 purging during intervals. An overall 100 h tests were carried out in H_2 mode. Interestingly, in H_2 mode, a current decay is observed from the beginning to the end of the test each day (i.e., from ~1.0 $A\cdot cm^{-2}$ to ~0.7 $A\cdot cm^{-2}$). However, the performance is recovered to its initial value after restarting the cell in the cycle following. The possible reason associated with this phenomenon is that the anode microporous structure is blocked by the in situ generated water during fuel cell operation. The performance recovery was observed due to the evaporation of H_2O during N_2 purging and cell resting period. At the end of the 100 h test, the fuel cell almost retained its initial behavior, as noted in *SI Appendix*, Fig. 26, demonstrating the excellent durability of the catalyst. Furthermore, we also tested the cell behavior of the CO-PEMFC with constant voltage hold at 0.65 V under 100 kPa CO-O_2. The IrRu-N-C catalyst showed only a 21.1% decay in current density after 140 h of continuous operation, indicating a sustainable stability in the CO-PEMFC. We then further validated the superiority of the IrRu-N-C catalysts toward HOR and COOR in PEMFC after the prolonged constant voltage test. As shown in *SI Appendix*, Fig. 27, the peak power densities of the H_2-PEMFC and CO-PEMFC were only slightly dropped by 8.5% and 9.6%, respectively. Combining the above results together, the IrRu-N-C is shown to exhibit good structure stability to withstand the PEMFC operating condition.

Enhancement Mechanism. We next combined the theoretical calculations with experimental tests to reveal the underlying origin of the antipoisoning feature of IrRu-N-C. As discussed above, water activation is a prerequisite for COOR; hence we first studied the decomposition process of H_2O based on density functional theory (DFT) calculations. To begin with, it is found that single IrN_4 and RuN_4 sites are incapable of water activation due to the overly high energy barrier (Fig. 4A) for the formation of adsorbed OH* through O-H bond cleavage (i.e., 1.92 eV for IrN_4 sites and 1.35 eV for RuN_4 sites, respectively). The ineffectiveness toward water activation makes the subsequent COOR unlikely to occur on a single site. Thus, given the strong synergistic effect between Ir and Ru in COOR according to experimental observation, we deduce that two single sites in close approach may work cooperatively to complete the reaction. Therefore, a MN_4-MN_4 (M = Ir or Ru) structure is adopted to model the two adjacent metal sites. Notably, all dual sites dissociate water exothermically with low energy barriers or even barrierless (*SI Appendix*, Table 8), thus conferring the catalysts with abundant OH functional groups, in line with EXAFS fitting results. Next, in order to probe into the adsorption and catalytic center for CO, we carried out temperature programmed desorption (CO-TPD) and diffuse reflectance infrared Fourier transform spectroscopy (CO-DRIFT) analysis. The results show that both Ir and Ru bind to CO at appreciable binding strength (Fig. 4B), with CO linearly bonded atop the
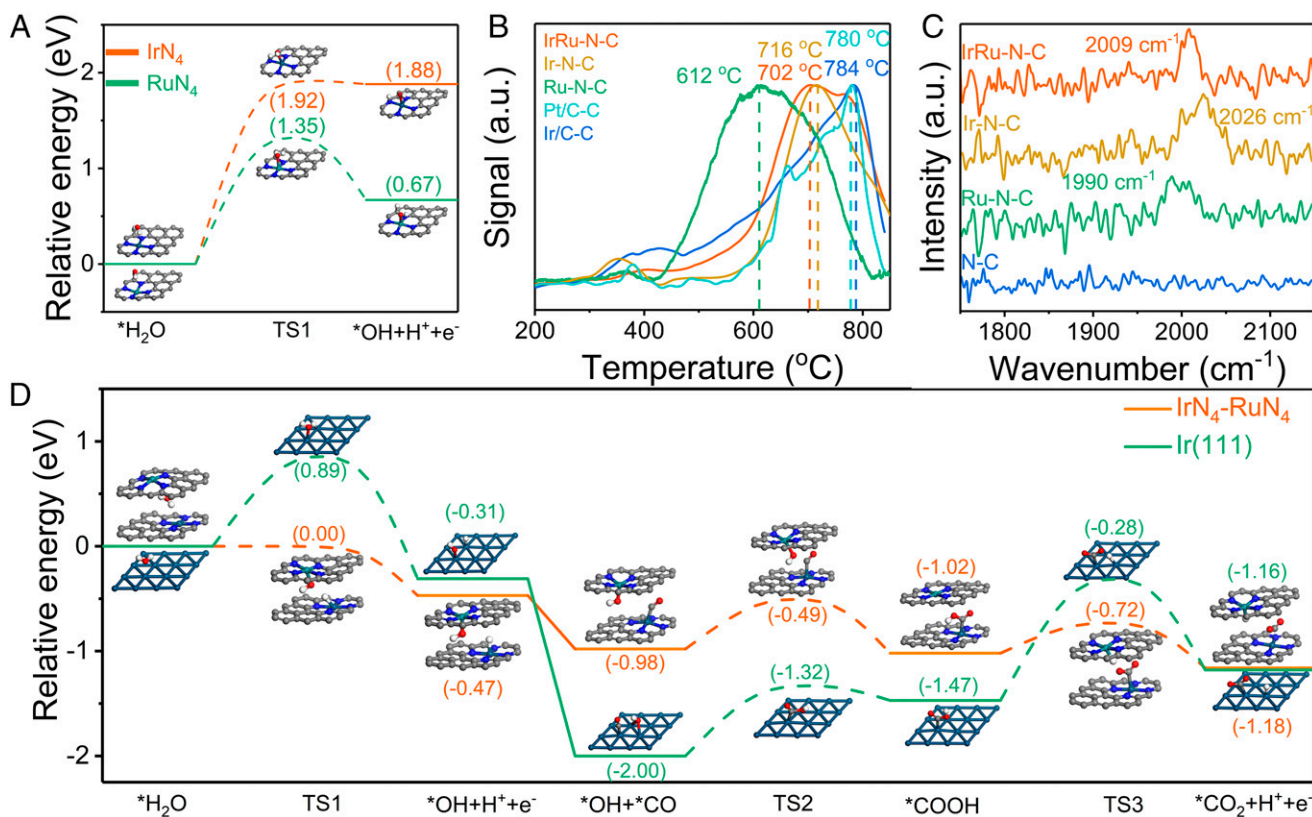
Wang et al.
Proton exchange membrane fuel cells powered with both CO and H_2

PNAS | 5 of 7
https://doi.org/10.1073/pnas.2107332118

Fig. 4. COOR reaction paths and CO adsorption status on the catalysts. (*A*) Energy profiles for H_2O dissociation on IrN_4 and RuN_4 surfaces. (*B*) CO-TPD for the as-prepared catalysts. (*C*) CO-DRIFT for the as-prepared catalysts. (*D*) Energy profiles for the entire CO oxidation process on IrN_4-RuN_4 and Ir(111) catalysts. The *x* axis shows the reaction intermediates and transition states (TSs); the *y* axis shows the relative energy of each state. Ir, Ru, N, C, O, and H atoms are shown in olive, dark green, blue, gray, red, and white, respectively.

site of the single centers according to CO-DRIFT (adsorption peak at 1,990 to 2,026 cm^{-1}, Fig. 4*C*) (43–45). The CO-TPD results (Fig. 4*B*) illustrate a slightly stronger CO adsorption on Ir-N-C (716 °C) versus Ru-N-C (612 °C), making CO more likely to adsorb on the Ir active center when the two sites are in close approach. We thus select this adsorption configuration to further model COOR process. Under this adsorption configuration, the adsorbed CO* (on Ir) and OH* (on Ru) combine at a fast pace to form COOH*, as it is an exothermic step (−0.04 eV) with the energy barrier at only 0.49 eV (Fig. 4*D*). The final deprotonation process to form CO_2 is also thermodynamically favored (−0.14 eV) with an even lower energy barrier at 0.30 eV. The synergy between RuN_4 and IrN_4 in water dissociation and CO oxidation gives this catalyst exceptional CO electrooxidation activity and antipoisoning feature, consistent with our experimental observation.

In order to elucidate the synergistic effect on the CO resistant feature, two homonuclear models of RuN_4-RuN_4 and IrN_4-IrN_4 were also calculated. The RuN_4-RuN_4 site, although effective toward water dissociation and CO adsorption, is completely ineffective toward COOR as the CO* + OH* step is a strong endothermic reaction (1.42 eV) unlikely to occur thermodynamically, in good agreement with our experimental observations. In contrast, the IrN_4-IrN_4 site seems effective toward COOR at the beginning; however, it has a strong tendency to sequentially dissociate water with energy barrier at only 0.56 eV, rendering the Ir sites easily covered by excessive OH (*SI Appendix*, Fig. 28). The axial OH not only reduces the active sites for CO adsorption but also makes the sequential CO* + OH* step thermally endothermic (0.8 eV) and hardly occurs. This explains the reason of low CO oxidation activity on the Ir-N-C catalyst in the

experiment. On metallic Ir(111), where CO binds to Ir sites strongly (CO-TPD at 784 °C), both water dissociation (energy barrier at 0.89 eV) and the COOH* to CO_2 (1.19 eV) conversion demonstrate high energy barriers, with the former process also being thermodynamically unfavorable (endothermic 0.31 eV). Therefore, the Ir/C is much less effective for H_2 oxidation in the presence of CO impurity than IrRu-N-C.

Discussion

We have developed a PEMFC anode catalyst that comprises Ru and Ir single-atom sites. This catalyst shows superb catalytic performance when using H_2, CO, or a combination of the two as fuels. The poisonous CO turns into a reactive fuel due to the interplay between approximated Ir and Ru sites, as the water dissociation and CO oxidation becomes extremely easy due to the coordination between the two sites. This catalyst paves the way toward a more robust PEMFC anode with a high antipoisoning feature.

Materials and Methods

Experimental details on synthesis and characterization of IrRu-N-C catalyst, including structure and electrochemical characterization, and the IrRu-N-C–based PEMFC measurements, and DFT calculation details on models are provided in *SI Appendix*.

Data Availability. All study data are included in the article and/or *SI Appendix*.

1. T. Ioroi, Z. Siroma, S.-i. Yamazaki, K. Yasuda, Electrocatalysts for PEM fuel cells. *Adv. Energy Mater.* **9**, 1801284–1808003 (2018).
2. H. Zhang, P. K. Shen, Recent development of polymer electrolyte membranes for fuel cells. *Chem. Rev.* **112**, 2780–2832 (2012).
3. V. Mehta, J. S. Cooper, Review and analysis of PEM fuel cell design and manufacturing. *J. Power Sources* **114**, 32–53 (2003).
4. B. Shabani, M. Hafttananian, S. Khamani, A. Ramiar, A. A. Ranjbar, Poisoning of proton exchange membrane fuel cells by contaminants and impurities: Review of mechanisms, effects, and mitigation strategies. *J. Power Sources* **427**, 21–48 (2019).
5. M. K. Debe, Electrocatalyst approaches and challenges for automotive fuel cells. *Nature* **486**, 43–51 (2012).
6. B. C. H. Steele, A. Heinzel, Materials for fuel-cell technologies. *Nature* **414**, 345–352 (2001).
7. A. Beniya, S. Higashi, Towards dense single-atom catalysts for future automotive applications. *Nat. Catal.* **2**, 590–602 (2019).
8. R. Bashyam, P. Zelenay, A class of non-precious metal composite catalysts for fuel cells. *Nature* **443**, 63–66 (2006).
9. W. Sheng et al., Non-precious metal electrocatalysts with high activity for hydrogen oxidation reaction in alkaline electrolytes. *Energy Environ. Sci.* **7**, 1719–1724 (2014).
10. Y. He, S. Liu, C. Priest, Q. Shi, G. Wu, Atomically dispersed metal-nitrogen-carbon catalysts for fuel cells: Advances in catalyst design, electrode performance, and durability improvement. *Chem. Soc. Rev.* **49**, 3484–3524 (2020).
11. R. Borup et al., Scientific aspects of polymer electrolyte fuel cell durability and degradation. *Chem. Rev.* **107**, 3904–3951 (2007).
12. L. Cao et al., Atomically dispersed iron hydroxide anchored on Pt for preferential oxidation of CO in H_2. *Nature* **565**, 631–635 (2019).
13. G. Shi, H. Yano, D. A. Tryk, A. Iiyarna, H. Uchida, Highly active, CO-tolerant, and robust hydrogen anode catalysts: Pt-M (M = Fe, Co, Ni) alloys with stabilized pt-skin layers. *ACS Catal.* **7**, 267–274 (2017).
14. T. Wang et al., Constructing canopy-shaped molecular architectures to create local Pt surface sites with high tolerance to H_2S and CO for hydrogen electrooxidation. *Energy Environ. Sci.* **11**, 166–171 (2018).
15. D. Wang et al., Highly stable and CO-tolerant $Pt/Ti_{0.7}W_{0.3}O_2$ electrocatalyst for proton-exchange membrane fuel cells. *J. Am. Chem. Soc.* **132**, 10218–10220 (2010).
16. H. A. Gasteiger, N. M. Markovic, P. N. Ross, H_2 and CO electrooxidation on well-characterized Pt, Ru, and Pt-Ru. 1. Rotating disk electrode studies of the pure gases including temperature effects. *J. Phys. Chem.* **99**, 8290–8301 (1995).
17. C. Roth et al., Determination of O[H] and CO coverage and adsorption sites on PtRu electrodes in an operating PEM fuel cell. *J. Am. Chem. Soc.* **127**, 14607–14615 (2005).
18. T. Takeguchi et al., Evidence of nonelectrochemical shift reaction on a CO-tolerant high-entropy state Pt-Ru anode catalyst for reliable and efficient residential fuel cell systems. *J. Am. Chem. Soc.* **134**, 14508–14512 (2012).
19. M. Arenz et al., Carbon-supported Pt–Sn electrocatalysts for the anodic oxidation of H_2, CO, and H_2/CO mixtures.Part II: The structure–activity relationship. *J. Catal.* **232**, 402–410 (2005).
20. H. A. Gasteiger, N. M. Markovic, P. N. Ross, Electrooxidation of CO and H_2/CO mixtures on a well-characterized Pt_3Sn electrode surface. *J. Phys. Chem.* **99**, 8945–8949 (1995).
21. M. Moses-DeBusk et al., CO oxidation on supported single Pt atoms: Experimental and ab initio density functional studies of CO interaction with Pt atom on θ-Al_2O_3(010) surface. *J. Am. Chem. Soc.* **135**, 12634–12645 (2013).
22. Z. Zhang et al., Thermally stable single atom Pt/m-Al_2O_3 for selective hydrogenation and CO oxidation. *Nat. Commun.* **8**, 16100 (2017).
23. Q. Fu, H. Saltsburg, M. Flytzani-Stephanopoulos, Active nonmetallic Au and Pt species on ceria-based water-gas shift catalysts. *Science* **301**, 935–938 (2003).
24. B. Qiao et al., Single-atom catalysis of CO oxidation using Pt_1/FeO_x. *Nat. Chem.* **3**, 634–641 (2011).
25. D. C. Papageorgopoulos, M. Keijzer, F. A. de Bruijn, The inclusion of Mo, Nb and Ta in Pt and PtRu carbon supported 3electrocatalysts in the quest for improved CO tolerant PEMFC anodes. *Electrochim. Acta* **48**, 197–204 (2002).
26. J.-H. Wee, K.-Y. Lee, Overview of the development of CO-tolerant anode electrocatalysts for proton-exchange membrane fuel cells. *J. Power Sources* **157**, 128–135 (2006).
27. J. Li et al., Atomically dispersed manganese catalysts for oxygen reduction in proton-exchange membrane fuel cells. *Nat. Catal.* **1**, 935–945 (2018).
28. M. Xiao et al., Engineering energy level of metal center: Ru single-atom site for efficient and durable oxygen reduction catalysis. *J. Am. Chem. Soc.* **141**, 19800–19806 (2019).
29. Z. Li et al., Iridium single-atom catalyst on nitrogen-doped carbon for formic acid oxidation synthesized using a general host-guest strategy. *Nat. Chem.* **12**, 764–772 (2020).
30. M. Xiao et al., A single-atom iridium heterogeneous catalyst in oxygen reduction reaction. *Angew. Chem. Int. Ed. Engl.* **58**, 9640–9645 (2019).
31. H. N. Nong et al., A unique oxygen ligand environment facilitates water oxidation in hole-doped $IrNiO_x$ core-shell electrocatalysts. *Nat. Catal.* **1**, 841–851 (2018).
32. Q. Wang et al., Coordination engineering of iridium nanocluster bifunctional electrocatalyst for highly efficient and pH-universal overall water splitting. *Nat. Commun.* **11**, 4246–4246 (2020).
33. Y. Y. Zhou et al., Lattice-confined Ru clusters with high CO tolerance and activity for the hydrogen oxidation reaction. *Nat. Catal.* **3**, 454–462 (2020).
34. Y. Duan et al., Bimetallic nickel-molybdenum/tungsten nanoalloys for high-efficiency hydrogen oxidation catalysis in alkaline electrolytes. *Nat. Commun.* **11**, 4789 (2020).
35. M. Zhou, C. Yang, K.-Y. Chan, Structuring porous iron-nitrogen-doped carbon in a core/shell geometry for the oxygen reduction reaction. *Adv. Energy Mater.* **4**, 1400840 (2014).
36. B. Lim et al., Pd-Pt bimetallic nanodendrites with high activity for oxygen reduction. *Science* **324**, 1302–1305 (2009).
37. U.S. DRIVE, Fuel Cell Technical Team Roadmap, https://www.energy.gov/sites/default/files/2017/11/f46/FCTT_Roadmap_Nov_2017_FINAL.pdf.
38. S. M. Brkovic et al., Non-stoichiometric tungsten-carbide-oxide-supported Pt-Ru anode catalysts for PEM fuel cells-From basic electrochemistry to fuel cell performance. *Int. J. Hydrogen Energy* **45**, 13929–13938 (2020).
39. T. Yamanaka, T. Takeguchi, G. Wang, E. N. Muhamad, W. Ueda, Particle size dependence of CO tolerance of anode PtRu catalysts for polymer electrolyte fuel cells. *J. Power Sources* **195**, 6398–6404 (2010).
40. T. Takeguchi, T. Yamanaka, G. Wang, E. N. Muhamad, W. Ueda, Structures and CO tolerance of anode PtRu catalysts for polymer electrolyte fuel cells. *ECS Trans.* **25**, 1319–1323 (2009).
41. S. Yamazaki, M. Yao, Z. Siroma, T. Ioroi, K. Yasuda, New-concept CO-tolerant anode catalysts using a Rh porphyrin-deposited PtRu/C. *J. Phys. Chem. C* **114**, 21856–21860 (2010).
42. I. X. Green, W. Tang, M. Neurock, J. T. Yates, Jr, Spectroscopic observation of dual catalytic sites during oxidation of CO on a Au/TiO_2 catalyst. *Science* **333**, 736–739 (2011).
43. H. Ziaei-Azad, N. Semagina, Bimetallic catalysts: Requirements for stabilizing PVP removal depend on the surface composition. *Appl. Catal. A Gen.* **482**, 327–335 (2014).
44. J. Shen, N. Semagina, Iridium- and platinum-free ring opening of indan. *ACS Catal.* **4**, 268–279 (2014).
45. G. Nagy et al., Selective aerobic oxidation of benzyl alcohol on alumina supported Au-Ru and Au-Ir catalysts. *Mol. Catal.* **492**, 110917 (2020).